Effect of Periodic Wake Passing on Film Effectiveness of Discrete Cooling Holes Around the Leading Edge of a Blunt Body

K. Funazaki

M. Yokota

Department of Mechanical Engineering,
Iwate University,
Morioka, Japan

S. Yamawaki

Aero-Engine & Space Operations,
Ishikawajima-Harima Heavy Industries,
Nishitama-gun, Tokyo, Japan

Detailed studies are conducted on film effectiveness of discrete cooling holes around the leading edge of a blunt body that is subjected to periodically incoming wakes as well as free-stream turbulence with various levels of intensity. The cooling holes have a configuration similar-to that of typical turbine blades except for the spanwise inclination angle. Secondary air is heated so that the temperature difference between the mainstream and secondary air is about 20 K. In this case, the air density ratio of the mainstream and secondary air becomes less than unity, therefore the flow condition encountered in an actual aero-engine cannot be simulated in terms of the density ratio. A spoke-wheel type wake generator is used in this study. In addition, three types of turbulence grids are used to elevate the free-stream turbulence intensity. We adopt three blowing ratios of the secondary air to the mainstream. For each of the blowing ratios, wall temperatures around the surface of the test model are measured by thermocouples situated inside the model. The temperature is visualized using liquid crystals in order to obtain qualitative information of film effectiveness distribution.

Introduction

To improve the performance of gas turbines, the specifications for turbine inlet temperature continue to increase while cooling air flow is kept to a minimum. For this reason, turbine cooling techniques must be improved not only for blades in the first stage but also for blades in the subsequent stages. Furthermore, those blade metal temperatures must be predicted more accurately.

Film cooling is an effective method for protecting blade surfaces from high temperature combustion gas. There have been many investigations to study film cooling on flat and curved surfaces for low mainstream turbulence intensities.

The leading edge of turbine blades is a prime area of concern in this study because the surface heat transfer coefficient around it is inherently high. In addition, since the boundary-layer thickness on the leading edge is thin, the free-stream turbulence and the periodic wake affect heat transfer very much.

Recently, Mehendale and Han (1992), using a blunt body with a circular leading edge as a test model, studied the effect of free-stream turbulence on film cooling effectiveness and the surface heat transfer coefficient, where secondary air was injected through two rows of inclined holes locating at ±15 and ±40 deg from the stagnation. Passive and jet grids generated several turbulence levels in the range of Tu = 5.07 – 12.9 percent. The leading edge Reynolds number was 100,000. They found that the leading edge film effectiveness for blowing ratio of 0.4 was significantly reduced by high free-stream turbulence. For blowing ratios of 0.8 and 1.2, the free-stream turbulence effect diminished at the leading edge but still existed on the flat sidewall region. They also pointed out that the effect of free-stream turbulence was more pronounced for ±15 deg one row injection than ±40 deg one row injection.

Abhari and Epstein (1994) studied heat transfer on a film cooled rotor blade, under simulated nondimensional engine conditions, with time-resolved measurements. They found that film cooling reduced the time-averaged heat transfer by as much as 60 percent on the suction side, but the effect on the pressure side was relatively limited one. Takeishi et al. (1992) compared the film effectiveness for a rotor blade with that for the corresponding stationary cascade under 4 percent free-stream turbulence intensity, using the heat-mass transfer analogy. They reported that in the leading edge region and on the suction surface, the film effectiveness for the cascade and rotor blade matched well, whereas on the pressure surface the cascade film effectiveness was higher. Although these two studies are useful, the effect of wakes and centrifugal force could not be isolated.

Mehendale et al. (1994) studied the effect of periodic wakes on film effectiveness and heat transfer on a model turbine blade with air or CO_2 film injection through three rows of film holes in the leading edge region and two rows each on the pressure and suction surfaces. They found that an increase in wake Strouhal number caused a decrease in film effectiveness values over most of the blade surface for both density ratios and at all blowing ratios. Since they used a model blade, they could not focus on the leading edge, which had the highest heat load.

Recently, Funazaki (1996) studied the influence of periodically passing wakes on the heat transfer over the leading edge as well as the flat plate. Local heat transfer distributions along the test surface were measured under the several unsteady conditions of bar-passing Strouhal number for four inlet Reynolds numbers. He found that the heat transfer along the surface of the test model was enhanced by the wakes with increasing Strouhal number. He derived a correlation and compared it with other experimental data. Using this correlation, his study yielded similar results to those of the previous studies concerning the wake effect, despite the large difference in the geometrical conditions.

Contributed by the International Gas Turbine Institute and presented at the 40th International Gas Turbine and Aeroengine Congress and Exhibition; Houston, Texas, June 5–8, 1995. Manuscript received by the International Gas Turbine Institute February 3, 1995. Paper No. 95-GT-183. Associate Technical Editor: C. J. Russo.

This study focuses on the effect of periodic passing wakes on the leading edge film cooling under several free-stream turbulence conditions using a blunt body with semi-circular leading edge and flat afterbody, which is similar to that of Mehendale et al. (1992) or Funazaki (1996). The present study is aimed at the investigation of the leading edge cooling effectiveness for turbine rotor blades or for stationary blades in the second or subsequent stages. The configurations of film holes are adopted from that of typical turbine blades, except for the spanwise inclination angle. All holes have their axes normal to the test model surface in consideration of applying the present results to the stationary blade case. This somewhat simplified configuration also helps us understand the effect of periodic wakes on film cooling, compared to the cases of spanwise inclined cooling holes. However, since we are aware of the necessity for investigation of more realistic cases, the succeeding study is now under way to examine the wake-affected film cooling effectiveness of 30 deg spanwise inclined cooling holes, which will be compared with the present results to examine the dependency of the unsteady effects on the inclination. The upstream periodic wake is produced by a spoke-wheel type wake generator like those used by Dullenkopf et al. (1991). The free-stream turbulence is generated by turbulence grids. We adopt three blowing ratios of the secondary air to the mainstream. For each of the blowing ratios, adiabatic wall temperature around the test surface subjected to the wakes as well as the free-stream turbulence is measured by thermocouples situated inside the test model. The effect of elevated free-stream turbulence on the wake-affected film effectiveness is also investigated. The temperature is visualized using liquid crystals in order to obtain qualitative information on the film effectiveness distribution.

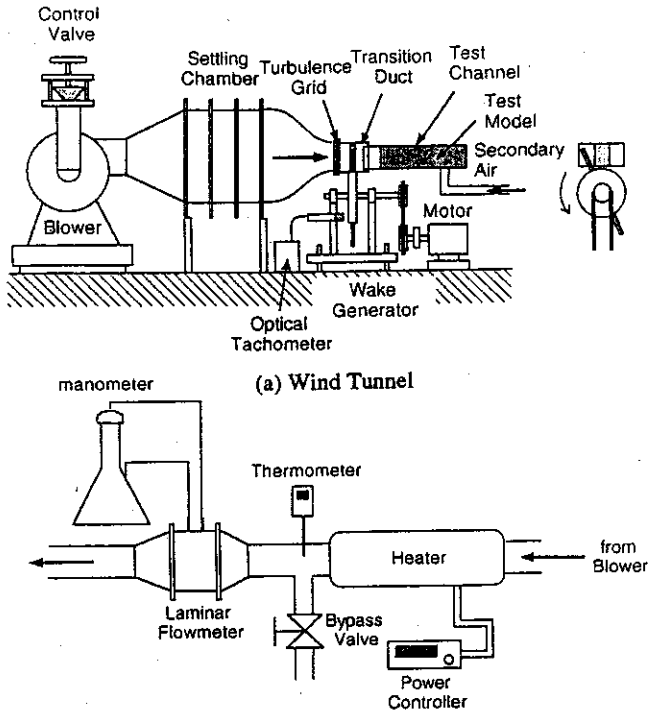

Fig. 1 Schematic layout of the test apparatus

Test Apparatus and Instrument

A schematic layout of the test apparatus is shown in Fig. 1. This apparatus is almost the same with one used in previous heat transfer test by Funazaki (1996), except for the secondary air supply system. The main flow rate is adjusted by the inlet valve of the blower. Air from the blower passes through a settling chamber to the contraction nozzle with the exit cross section of 240 mm × 350 mm. The test channel containing the test model is inserted into the transition duct, which is attached to the contraction nozzle. To remove the upstream boundary layer, the front portion of the test channel has a sharp-edged and 10 mm clearance with the transition duct. It also has a slot, through which the wake-generating bars can pass. The wake-generating bars, of 5 mm diameter and 250 mm length, are mounted on a disk rim. The rotational speed of the disk is controlled by transmission gear box connected to an induction motor. The rotational speed, ranging from 900 through 1500 rpm, is monitored by an optical tachometer and a stroboscope is also used to check the fluctuation of the rotation. Although the inertia of the disk is large enough to maintain a nearly constant rotational speed, a slight vibration of the cylinder bar and some structural vibration was observed. It didn't seem to drastically alter the wake, however. A turbulence grid is attached to the contraction nozzle exit, which is 300 mm upstream of the test model leading edge and 100 mm upstream of the wake generator. Three types of grid are used and details

Nomenclature

B = mean blowing ratio = $\rho_2 U_2 / \rho_\infty U_\infty$
B_{15}, B_{40} = local blowing ratio
D = leading edge diameter
d = cooling hole diameter
d_g = diameter of the turbulence grid wire
f = wake passing frequency = $nn_c/60$
L = axial gap between the turbulence grid and the model leading edge
L_e, $L_{e,w}$ = streamwise dissipation length of free-stream turbulence and wake turbulence
M = grid mesh size of the turbulence grid
M_{15}, M_{40} = local momentum ratio
Nu_D = Nusselt number based on the leading edge diameter
n, n_c = rotating speed and the number of wake generating bars
R = radius of the leading edge
Re_D = Reynolds number based on the diameter of the leading edge and the inlet velocity = $U_\infty D/\nu$
S = Strouhal number = fD/U_∞
T, T_{aw} = temperature, adiabatic wall temperature
$Tu(t)$ = turbulence intensity
Tu_b = background turbulence intensity
U_{local} = local flow velocity around the model surface
U_∞ = inlet velocity
u' = streamwise velocity fluctuation
V_{out} = outlet velocity
v = velocity on the model surface
$v_j(t)$, $\tilde{v}(t)$ = unsteady velocity, ensemble-averaged velocity
X = streamwise distance measured from the wake generating bar
X_G = streamwise distance measured from the turbulence grid
x = axial distance measured from the leading edge
x_{surf} = distance along the surface from the stagnation on the leading edge
η = film effectiveness = $(T_{aw} - T_\infty)/(T_2 - T_\infty)$

Subscripts

∞, 2 = mainstream, secondary air
15, 40 = first row, second row

Table 1 Configurations of turbulence grids characteristics

	Grid 1	Grid 2	Grid 3
Wire Diameter(dg)	0.8 mm	1.9 mm	5.0 mm
Mesh Width (M)	5.0 mm	10.0 mm	30.0 mm
Degree of Openness	0.70	0.66	0.69
M/dg	6.25	5.26	6.00
Tu_b (Eq.(7))	1.5%	2.2%	4.0%

of the grid configurations are shown in Table 1. Although the turbulence intensity attainable with these "passive type" grids at the test model location is at most 4 percent as demonstrated later, it appears high enough to simulate the inlet flow condition to a turbine rotor blade. This can be justified for the first-stage rotor considerating the flow acceleration through the first-stage nozzle, and a corresponding inlet turbulence intensity to the first stage nozzle of about 10 percent.

The secondary air, which is supplied to the film hole on the leading edge of the test model, is heated before a laminar flow meter. Accordingly, the film air temperature is higher than the free-stream temperature, so that we cannot completely simulate the situation in an actual engine.

The cross section of the test channel is 200 mm high and 300 mm wide and its length is 1000 mm. The test model consists of a semi-circular leading edge of 100 mm diameter and a flat afterbody, shown in Fig. 2. The test model is assembled with acrylic-resin parts of 10 mm thickness and 200 mm height. Two rows of holes of d = 10 mm diameter and 40 mm ($4d$) pitch, located at ±15 and ±40 deg angled with the test model centerline. The ratio of the leading edge diameter and the cooling hole diameter, D/d is 10, We will refer to the film holes at ±15 and ±40 deg as "the first row" and "the second row," respectively.

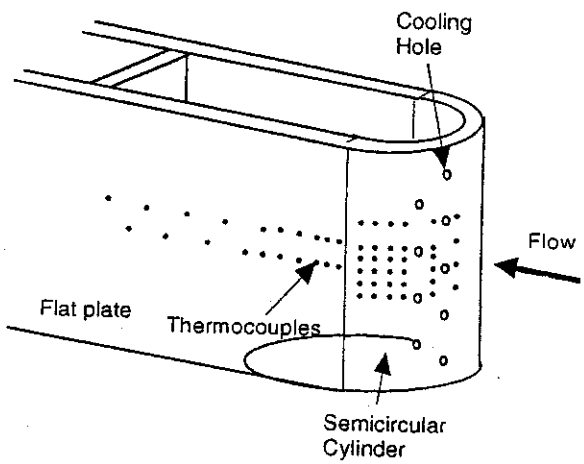

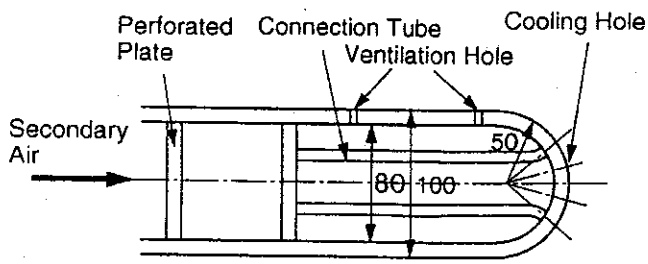

Fig. 2 Test model

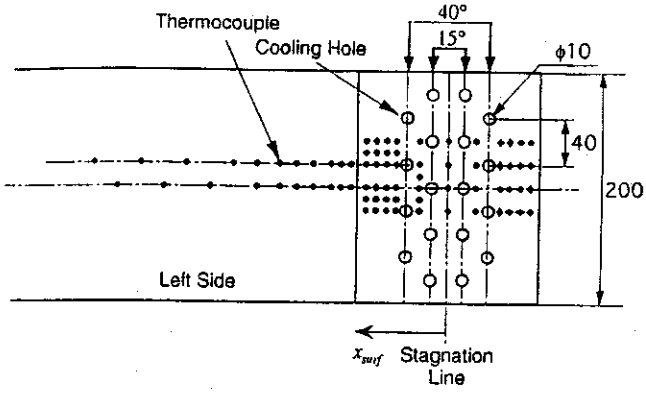

Fig. 3 Layout of thermocouples and film holes (unfolded surface view)

The secondary air is supplied from the flow distribution chamber inside the model to the holes through vinyl tubes. The vinyl tubes are insulated to prevent heat loss. Figure 3 shows the location of thermocouples and film holes. To measure an adiabatic surface temperature distribution, 74 thermocouples are embedded on the model surface. The secondary air temperature is measured near the hole exit. The surrounding temperature around the tubes is also measured. Free-stream temperature is measured near the lower end of the leading edge stagnation line. To prevent temperature increase inside the model, two ventilation holes are located on the flat plate of the model opposite to the test surface. All thermocouples are connected to a datalogger controlled by a personal computer.

These temperature data are then averaged over 10 samples acquired within a few minites to calculate time-averaged wall temperature distributions. To visualize the temperature distribution, liquid crystal sheets of 0.1 mm thickness (RW3040; Nippon Capsule Products) are attached to the model surface after the measurements with the thermocouples. The color changes in a temperature range of 30 ~ 40°C.

Pressure distributions around the test model are obtained using the test model of the same dimensions with the present one except for cooling holes, as had been employed by Funazaki (1996). Local flow velocity U_{local} is then determined from those data.

Experiment

In the present study, normalized parameters adopted in this study, except for Mach number, compare with those encountered in a real turbomachine as shown in Appendix A.

The inlet free-stream velocity was 20 m/s and the Reynolds number Re_D was 141,000. The rotational speeds of the wake generator were 900, 1260, and 1500 rpm. The corresponding Strouhal numbers, defined as

$$S = \frac{(nn_c/60)D}{U_\infty}, \tag{1}$$

were 0.22, 0.31 and 0.37.

Unsteady velocity measurements were conducted using a hot-wire anemometer. Several series of unsteady velocity data $v_j(t)\{j = 1, \ldots, m\}$ are processed to calculate the ensemble-averaged velocity $\tilde{v}(t)$

$$\tilde{v}(t) = \frac{1}{m}\sum_{j=1}^{m} v_j(t) \tag{2}$$

where m = 256. The time-resolved turbulence intensity used in this study is defined as the ensemble-averaged variance and calculated by

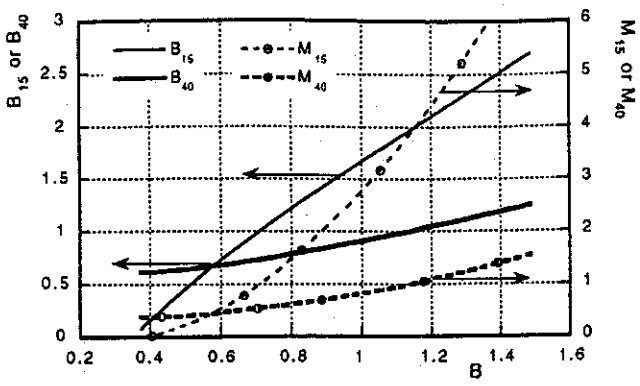

Fig. 4 Relationship of local and mean blowing ratio

$$Tu(t) = \frac{\frac{1}{m-1}\sum_{j=1}^{m}(v_j(t) - \bar{v}(t))^2}{U_{\text{local}}} \tag{3}$$

The blowing ratio B, the dominant parameter for film cooling, is defined as

$$B = \frac{\rho_2 U_2}{\rho_\infty U_\infty}. \tag{4}$$

B is based on the mean secondary air and the inlet flow mass flux. All experiments were conducted at the mean blowing ratios, B = 0.4, 0.8, or 1.2. Although this blowing ratio is a convenient parameter for this type of experiment, local blowing ratio at each row is more useful for understanding the local film cooling performance. The local blowing ratio is defined as

$$B_{15} = \frac{\rho_{2,15}U_{2,15}}{\rho_{\infty,15}U_{\infty,15}}, \quad B_{40} = \frac{\rho_{2,40}U_{2,40}}{\rho_{\infty,40}U_{\infty,40}}. \tag{5}$$

Figure 4 shows the analytical result of the relationship between the local and mean blowing ratios, as well as the relationship between the local momentum ratio and mean blowing ratios. Readers can refer to Appendix B for more detail. Notice that these relationships differ for each row. For instance, for B_{15}, the slope of the curve is about 2.5 and $B_{15} \gg 1$ when $B \geq 0.8$. In contrast, for B_{40}, the slope is about 0.5 and $B_{40} \leq 1$ even when $B \leq 1.2$.

Film effectiveness η is defined as

$$\eta = \frac{T_{aw} - T_\infty}{T_2 - T_\infty}, \tag{6}$$

where T_{aw} is the adiabatic wall temperature, T_2 is the secondary air temperature, and T_∞ is mainstream temperature. During the experiment, the temperature difference $T_{aw} - T_w$ was maintained about 20 K. To give the model a sufficiently adiabatic condition, a temperature increase inside the model was limited by two ventilation holes described previously. The temperature inside the model was therefore maintained only 5–6 K higher than mainstream temperature, which was nearly equal to the average temperature around the outer surface of the model. It can be consequently expected that such a small difference in temperature between both sides of the plate yielded almost adiabatic condition of the model surface except near the film holes.

An uncertainty analysis based on the method of Kline and McClintock (1953) was carried out for the film effectiveness. The uncertainty of film effectiveness is about 4.5 percent near the film holes and less than 9.7 percent for downstream.

Results and Discussion

Velocity Distribution. Figure 5 shows the velocity distribution around the leading edge of the test model. In this figure, the results of a potential flow analysis by use of BEM (Boundary Element Method) are compared with the measurement data. The heat transfer distribution ($Nu_D/Re_D^{0.5}$) is also plotted (Funazaki, 1996). Velocity distributions are the same on both sides of the leading edge, showing the symmetry of the flow field with respect the model center line. These data show that there was a separation bubble around the junction of leading edge and flat plate. The separation began at $X_{surf}/R \cong 1$ and reattached at $X_{surf}/R \cong 2$. Velocity fluctuations were not discernible even under the influence of the wakes, since these distributions were measured by a slow response Betz manometer. It does not seem from this figure that the velocity distributions change drastically even when periodic wakes exist in the mainstream. However, we are aware of the importance of unsteady effects on the separated flow structure and the next projects concerning the unsteady effects are under way, but this is beyond the scope of the present study.

Free-Stream Turbulence. Figure 6 shows the free-stream turbulence measured at 200 mm upstream of the leading edge by use of a hot-wire anemometer. In order to avoid the influence of the model-disturbed flow field during this measurement as well as wake measurements described next, the test model was moved downstream by 200 mm from the nominal position so that the distance from the turbulence grid to the leading edge of the model was 500 mm. Note that streamwise traversing of the hot-wire probe could not be conducted due to a structural restriction of the test section. Therefore, only three data points are plotted in this figure against the streamwise distance normalized on the mesh width of the turbulence grid, X_G/M. Also cited are some of the results of Kestin and Wood (1971) for $M/d_g = 3.0$.

Although larger M/d_g in the present case provides lower turbulence intensities compared to those of Kestin and Wood, the present data tend to align along a line on the logarithmic diagram like the data of Kestin and Wood, where this line can be expressed by

$$Tu_b = 10.64(X_G/M)^{-0.559}, \quad M/d_g = 6 \tag{7}$$

Considering that the turbulence grids adopted here have almost the same values of M/d_g ($\cong$6), it seems possible to use Eq. (7) to predict the streamwise decay of the turbulence from each of the grids.

On the other hand, as pointed out by Kestin and Wood (1971) or Mehendale and Han (1992), the free-stream turbulence intensity rapidly increases near the stagnation of the test model. For the purpose of determining a reference turbulence intensity to the test model, Funazaki et al. (1995) derived the following expression for describing the behavior of turbulence intensity along the stagnation streamline, combining Eq. (7) with the solution of the potential flow field near the stagnation:

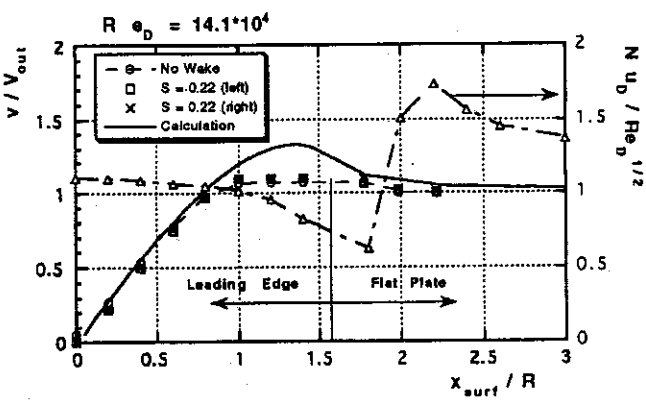

Fig. 5 Velocity and heat transfer distribution around the leading edge

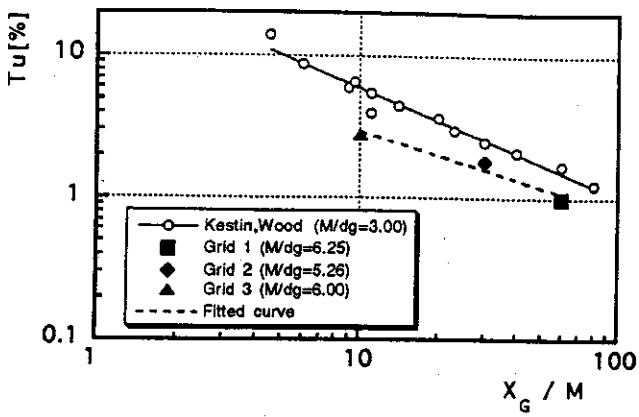

(a) The decay of free stream-turbulence

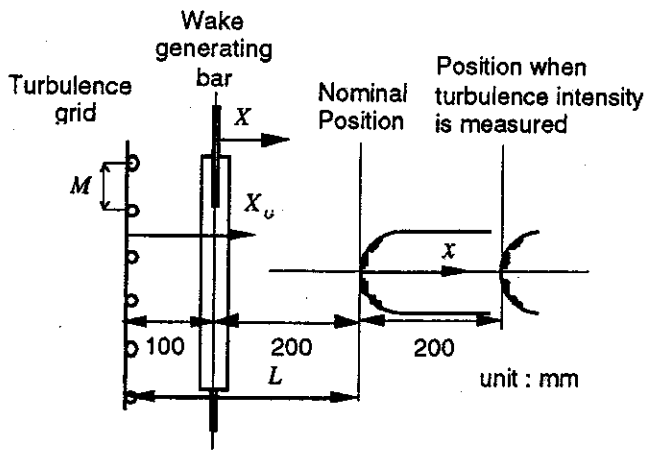

(b) Nomenclature

Fig. 6 The decay of free-stream turbulence

$$Tu_b(x) = 10.64\left(\frac{L - |x|}{M}\right)^{-0.559} \times \frac{1}{1 - (R/(x - R))^2} \quad (8)$$

In the nominal setting of the test model L was 300 mm, from which the minimum free-stream turbulence intensity was estimated as shown in Table 1. Like Mehendale et al. (1991), we hereafter use these minimum values as reference turbulence intensity.

As for length scale of the free-stream turbulence, a streamwise turbulence dissipation scale L_e, defined as (Hancock and Bradshaw, 1983)

$$L_e = -\frac{(\bar{u}'^2)^{3/2}}{U d\bar{u}'^2/dx} \quad (9)$$

was calculated by Eq. (7). As a result, at X_G = 300 mm we have L_e = 2.8 mm, 4.2 mm, and 7.8 mm for Grid 1, Grid 2, and Grid 3, respectively.

Wake Measurements. The measurement of unsteady velocity fluctuation were carried out using a hot wire anemometer, the details being described by Funazaki et al. (1995). Figure 7 shows some of the results about velocity and turbulence intensity measured 5 mm upstream of the leading edge stagnation with and without grid. The periodic wakes provide periodic increases of turbulence intensity. Care must be paid to more than 20 percent turbulence intensities occurring within the wakes, which are due to the reduced free-stream velocity near the model leading edge. Upstream of the test model, maximum turbulence intensity in the wake was 8 percent at most. The ensemble-averaged velocity increased slightly when the wakes were passing, probably due to the wake deformation near the blunt leading edge. Random peaks of Tu after the wake passed also appeared. Even when the turbulence grid was inserted in the upstream, the maximum value of Tu did not change but the amplitude of Tu decreased.

From these measurements, Funazaki et al. (1995) derived the following correlation for streamwise decay of turbulence intensity in the wake,

$$Tu_{max} = 73.58\left(\frac{X}{d}\right)^{-0.67} \quad (10)$$

Although this correlation, irrespective of wake passing Strouhal number, actually contains some amount of scatter, it is useful to understand the generic trend of the wake turbulence decay.

For convenience in the later discussion, we determine a streamwise turbulence dissipation length scale of the wake turbulence, $L_{e,w}$ from Eq. (9) in conjunction with Eq. (10) likewise in the case for free-stream turbulence. It follows that $L_{e,w}$ = 9.2 mm at X = 200 mm, which corresponds to X_G = 300 mm.

Film Effectiveness

The Wake Effect With No Turbulence Grid. Figures 8, 9 and 10 show spanwise averaged film effectiveness distributions for three wake Strouhal numbers as well as "no wake" condition with low free-stream turbulence (no grid). These figures

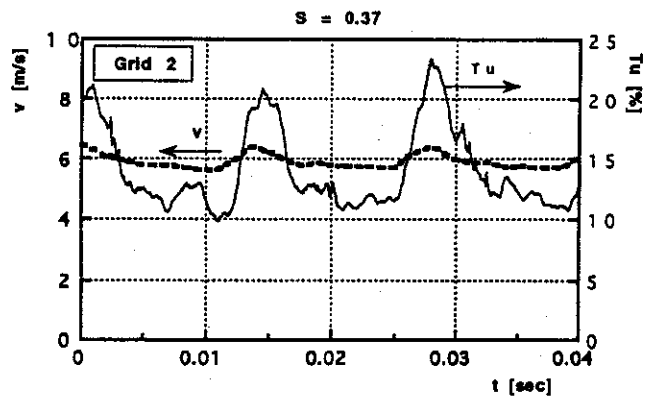

(a) No grid

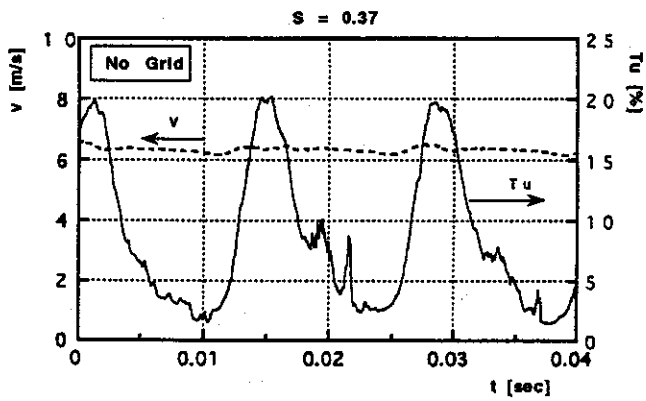

(b) With grid

Fig. 7 Unsteady velocity and turbulence profiles at 5 mm upstream of the leading edge with and without grids

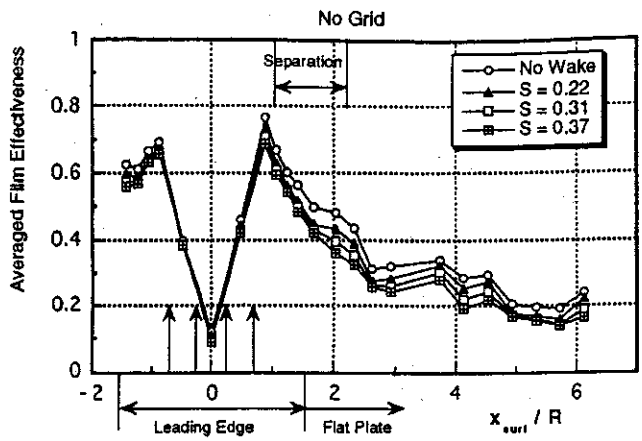

Fig. 8 Averaged film effectiveness without turbulence grid (B = 0.4)

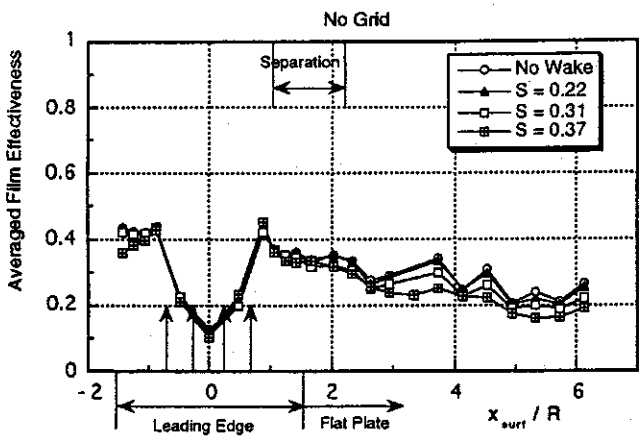

Fig. 9 Averaged film effectiveness without turbulence grid (B = 0.8)

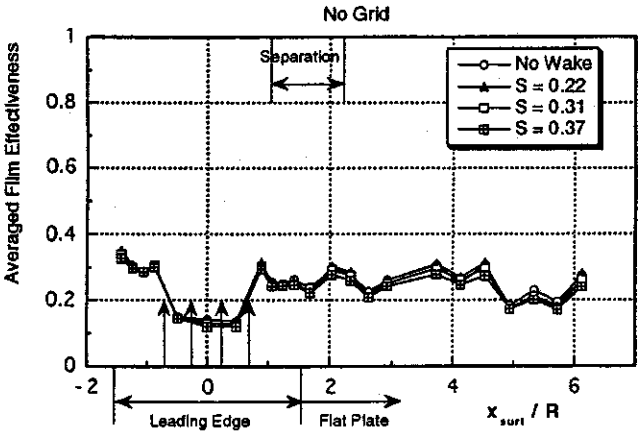

Fig. 10 Averaged film effectiveness without turbulence grid (B = 1.2)

differ by the mean blowing ratio, B, which is 0.4, 0.8, and 1.2, respectively. The position of the first row of film holes is at $X_{surf}/R = 0.262$ and at 0.698 for the second row. In these figures, the location of the separation bubble is also indicated on a basis of the "no wake" and "no grid" heat transfer data. In each case, film effectiveness has a peak value just after the second row of film holes. In $X_{surf}/R > 3$, all data show a slight fluctuation, because thermocouples are staggered as shown in Fig. 2.

The maximum film effectiveness appeared at $B = 0.4$, but its film effectiveness decreased rapidly downstream thereafter.

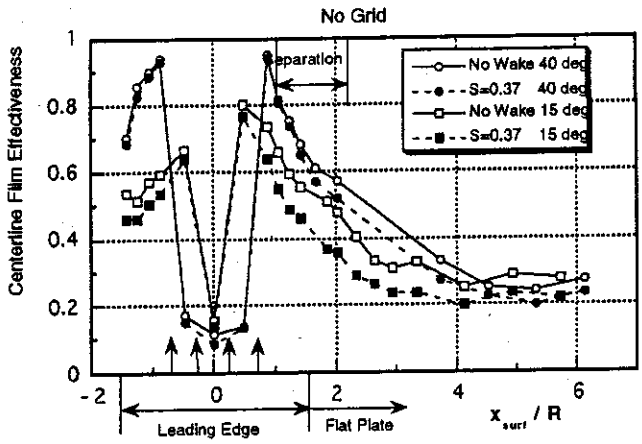

(a) B=0.4

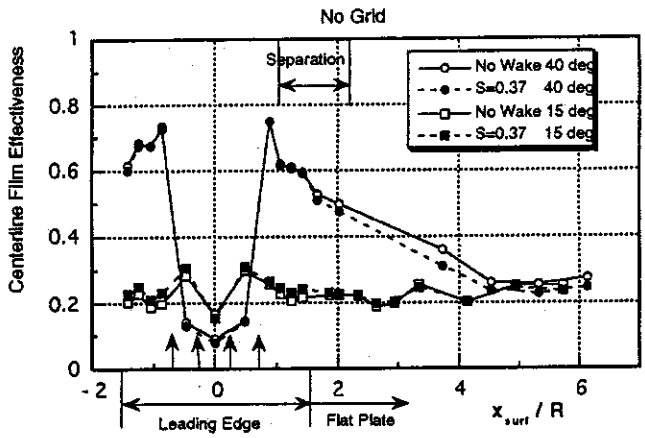

Fig. 11 Local film effectiveness without the turbulence grid

At $B = 1.2$, film effectiveness distribution was nearly flat (η = 0.2 to 0.3). Far downstream, $X_{surf}/R > 4$, film effectiveness was almost same for all blowing ratios.

The effect of periodic wakes on film effectiveness was larger for the lower blowing ratio cases. For example, at $B = 0.4$ the maximum decrease of film effectiveness by the wake was more than 0.1, while at $B = 1.2$ the effect of wakes was indistinguishable.

Figure 11(a, b) shows local film effectiveness distributions in the low and middle blowing ratio cases, respectively. In these figures, centerline film effectiveness distributions for each row are plotted with and without wakes. For $B = 0.4$, the effect of wakes for the first row caused a decrease of spanwise-averaged effectiveness as was also seen in Fig. 8. For $B = 0.8$, the effectiveness of the first row was low everywhere. In contrast, for the second row, a decrease of film effectiveness appeared only for $x_{surf}/R > 2$ in both blowing ratio cases.

There is a reasonable explanation why the first row centerline film effectiveness was significantly affected by the periodic wakes and blowing ratio. When $B = 0.4$, the local blowing ratio, B_{15}, was about 0.2 (refer to Fig. 4). At this very low local blowing ratio, film air easily attached to the surface; therefore, the film effectiveness was high. However, the film air also had quite low momentum and low turbulence compared to the surrounding air flow, which made it easy for the turbulence of periodic wakes to interact with the film air. In the case of B = 0.8, on the contrary, the local blowing ratio for the first row was $B_{15} \cong 1.2$ so that blow-off occurred, which resulted in low effectiveness. On the other hand, the local blowing ratio of the

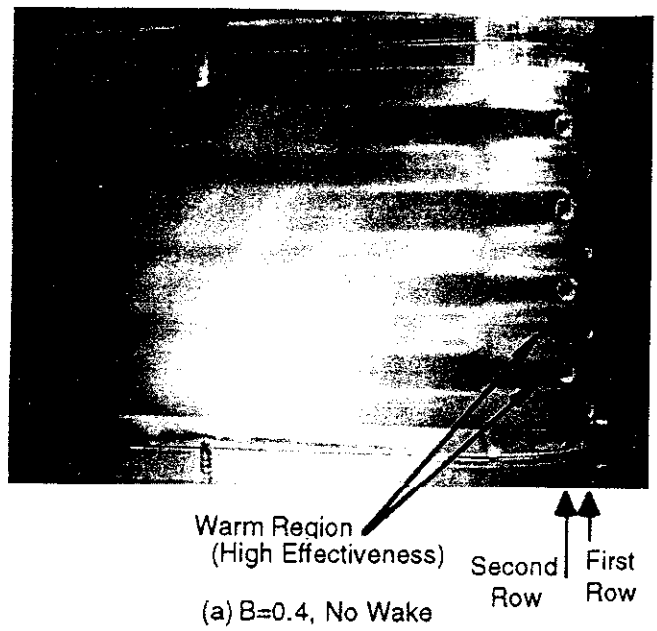

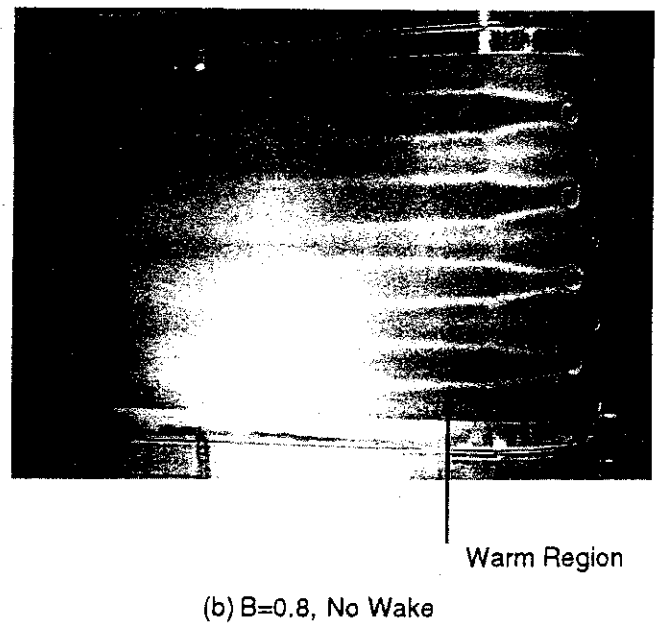

Fig. 12 Detailed temperature distribution around film holes

second row, B_{40}, changed slowly from 0.6 to 0.8 when B changed from 0.4 to 0.8 as shown in Fig. 4. Since B_{40} remained sufficiently low, the film air attached to the surface. The momentum of the second row air was also high enough that the turbulence from the periodic wakes could not affect the film air, especially near the film holes.

Figure 12 shows detailed temperature distribution around film holes through which heated secondary air was injected. Remember that the air was supplied to all the holes at the same time. There were high-temperature regions (high film effectiveness) downstream of both the first and second rows at $B = 0.4$. For higher blowing ratio, no warm regions downstream of the first row were confirmed because of the blow-off.

The Effect of Free-Stream Turbulence and Wakes. Figures 13, 14, and 15 show the spanwise-averaged film effectiveness obtained for three cases of free-stream turbulence intensity with three blowing ratios, respectively. There were no wakes in these cases. The manner in which the film effectiveness changed with

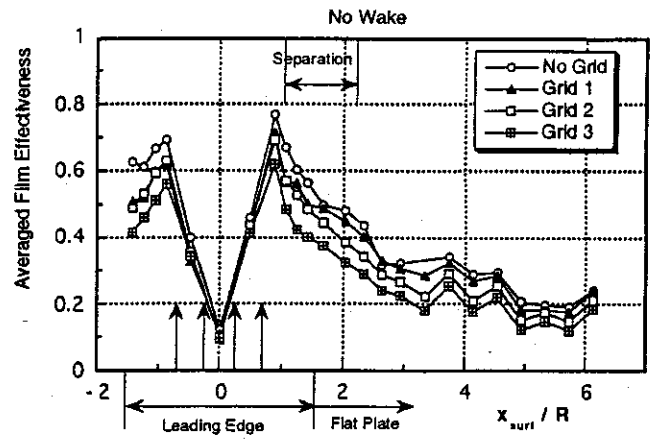

Fig. 13 Averaged film effectiveness without the wake effect (B = 0.4)

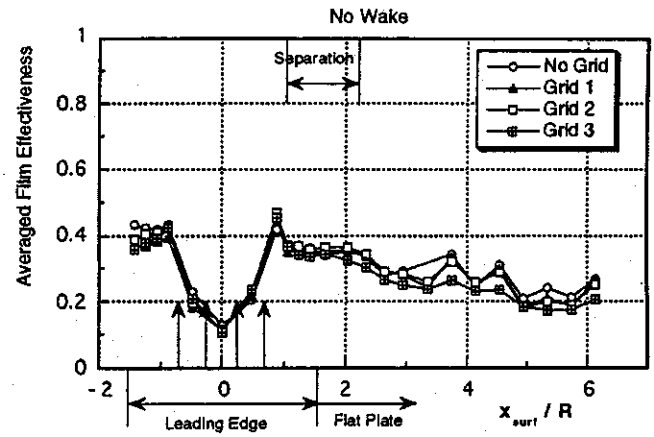

Fig. 14 Averaged film effectiveness without the wake effect (B = 0.8)

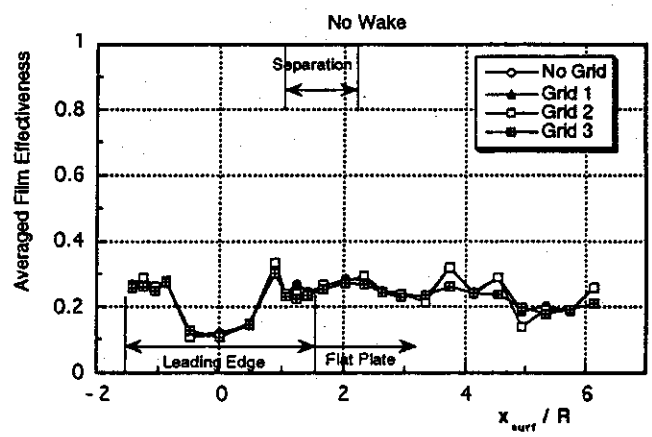

Fig. 15 Averaged film effectiveness without the wake effect (B = 1.2)

increase in free-stream turbulence resembles that of increasing the wake Strouhal number. At the lower blowing ratio, B = 0.4, the effect of free-stream turbulence on the film effectiveness was evident. The maximum reduction of effectiveness was about 0.2. For the case of no grid in Fig. 13, there appeared a region where the effectiveness distribution somewhat plateaued at about $x_{surf}/R = 3$ in the neighborhood of reattachment. This flat distribution disappeared as the turbulence intensity increased. It is not clear at this moment how the separation affected the film air flow; however, it is conceivable that some fraction of the secondary air was caught in the separation bubble

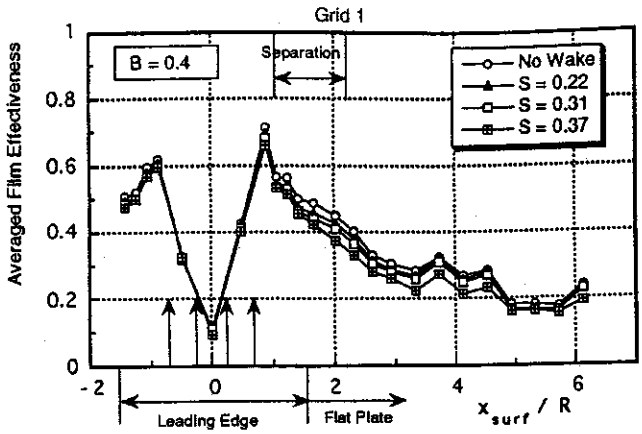

Fig. 16 Averaged film effectiveness with wake and free-stream turbulence effect (B = 0.4, Grid 1)

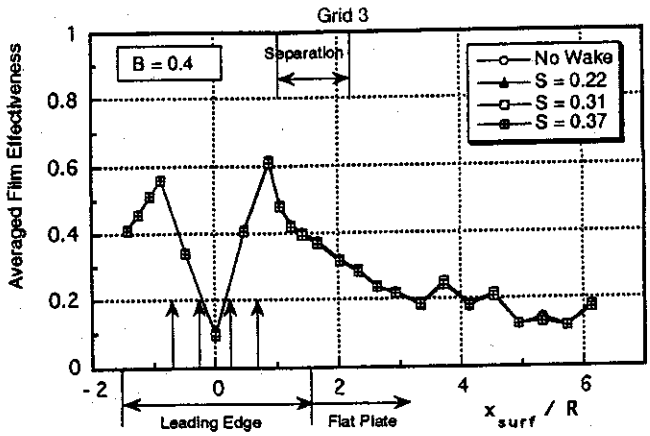

Fig. 18 Averaged film effectiveness with wake and free-stream turbulence effect (B = 0.4, Grid 3)

in the low free-stream turbulence case (no grid) and warm air stayed there for a relatively longer time.

Mehendale and Han (1992) conducted their study at almost the same conditions. Under low free-stream turbulence, the present film effectiveness for low blowing ratio, $B = 0.4$, agrees with their results well. Although the trend of decrease in film effectiveness with increasing blowing ratio also agrees, the present data shows lower effectiveness for high blowing ratio. This difference may be attributed to the difference in hole inclination angle. Their angle was 30 deg, while the holes in this study were normal to the surface. They also indicated that the film effectiveness for low blowing ratio ($B = 0.4$) decreased dramatically with increasing free-stream turbulence. Although this trend agrees with the present study, their data showed a more rapid decrease at higher blowing ratios.

The effects of periodic wakes on film effectiveness under the enhanced free-stream turbulences are shown in Figs. 16, 17, and 18, respectively. Only the results for the low blowing ratio case are shown here because they clearly show the effect of wake and turbulence. Although effectiveness decreased as wake Strouhal number increased, there was no wake effect at the highest free-stream turbulence. One might wonder why the periodic wakes of over 20 percent turbulence intensity as seen in Fig. 7 had almost no further impact on the film effectiveness in Fig. 18. One reason for this phenomenon is that the corresponding maximum turbulence intensity in the wake at the upstream was actually 8 percent at most. The other reason is that the observed wake duration relatively decreased compared to one wake passing period under the enhanced background turbulence, which weakened the wake effect. Furthermore, the effect of turbulence length scale cannot be dismissed. As shown previously, the streamwise turbulence dissipation length scale of the free-stream turbulence generated by Grid 3 ($L_e/D = 0.078$) was comparable to that of the wake turbulence ($L_e/D = 0.092$), which could be another possible reason for the reduction of the wake effect by the enhanced free-stream turbulence.

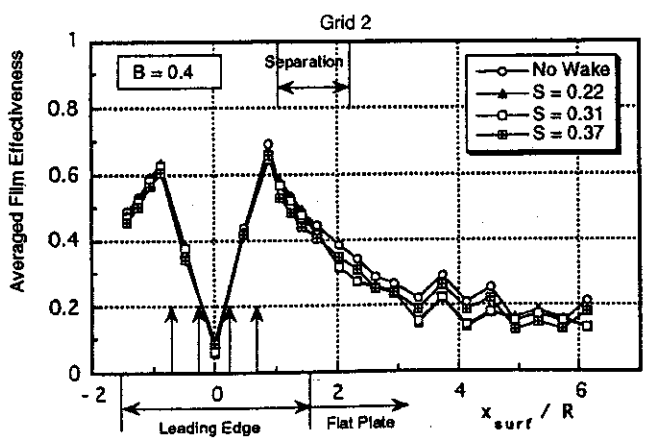

Fig. 17 Averaged film effectiveness with wake and free-stream turbulence effect (B = 0.4, Grid 2)

Conclusions

Detailed studies were conducted on film effectiveness of discrete film holes around the leading edge of a blunt body that was subjected to periodically incoming wakes as well as free-stream turbulence with various levels of intensity. Several important findings, useful for designing film-cooled turbine blades, were then obtained through the studies. The findings are summarized as follows:

1 In the range of this experiment, spanwise-averaged film effectiveness became highest at the blowing ratio of 0.4, because injected air from both the first and second rows attached to the surface.

2 For $B > 0.8$, the local blowing ratio for the first row was so high that the injected air blew off. This resulted in low film effectiveness downstream of the first row and deteriorated spanwise-averaged film effectiveness.

3 When a periodic wake impinged on the blunt body, film effectiveness decreased with increase of wake Strouhal number. The film effectiveness decreased most at the lowest mean blowing ratio, $B = 0.4$, because very low-momentum air injected from the first row was considerably susceptive to the wake.

4 Film effectiveness decreased with increase in free-stream turbulence, which diminished the effect of periodic wakes. This phenomenon could be attributed to the roles of the turbulence intensity as well as the turbulence length scale.

Acknowledgments

The authors are greatly indebted to Mr. K. Koizumi of Iwate University for his effort in executing the experiment and Dr. R. Henk of IHI for his review of this paper.

References

Abhari, R. S., and Epstein, A. H., 1994, "An Experimental Study of Film Cooling in a Rotating Transonic Turbine," ASME JOURNAL OF TURBOMACHINERY, Vol. 116, pp. 63–70.

Dullenkopf, K., Schulz, A., and Wittig, S., 1991, "The Effect of Incident Wake Conditions on the Mean Heat Transfer of an Airfoil," ASME JOURNAL OF TURBOMACHINERY, Vol. 113, pp. 412–418.

Funazaki, K., Yamawaki, S., and Maya, T., 1995, "Studies on Wake-Affected Heat Transfer Around the Leading Edge a Blunt Body," to be published in *Proc. 4th ASME–JSME Thermal Engineering Joint Conference.*

Funazaki, K., 1996, "Studies on Wake-Affected Heat Transfer Around the Circular Leading Edge of Blunt Body," ASME JOURNAL OF TURBOMACHINERY, Vol. 118, pp. 452–460.

Goebel, S. G., Abuaf, N., Lovett, J. A., and Lee, C. P., 1993, "Measurement of Combustor Velocity and Turbulence Profiles," ASME Paper No. 93-GT-228.

Hancock, P. E., and Bradshaw, P., 1983, "The Effect of Free-Stream Turbulence on Turbulent Boundary Layers," ASME *Journal of Fluids Engineering*, Vol. 105, pp. 284–289.

Kestin, J., and Wood, R., 1971, "The Influence of Turbulence on Mass Transfer From Cylinders," ASME *Journal of Heat Transfer*, Vol. 93, pp. 321–327.

Kline, S. J., and McClintock, F. A., 1953, "Describing Uncertainties in Single Sample Experiments," *Mechanical Engineering*, Vol. 75, pp. 3–8.

Mehendale, A. B., Han, J. C., and Ou, S., 1991, "Influence of High Mainstream Turbulence on Leading Edge Heat Transfer," ASME JOURNAL OF TURBOMACHINERY, Vol. 113, pp. 843–850.

Mehendale, A. B., and Han, J. C., 1992, "Influence of High Mainstream Turbulence on Leading Edge Film Cooling Heat Transfer," ASME JOURNAL OF TURBOMACHINERY, Vol. 114, pp. 707–715.

Mehendale, A. B., Han, J. C., Ou, S., and Lee., C. P., 1994, "Unsteady Wake Over a Linear Turbine Blade Cascade With Air and CO_2 Film Injection: Part II—Effect on Film Effectiveness and Heat Transfer Distributions," ASME JOURNAL OF TURBOMACHINERY, Vol. 116, pp. 730–737.

Ou, S., Mehendale, A. B., and Han, J. C., 1992, "Influence of High Mainstream Turbulence on Leading Edge Film Cooling Heat Transfer: Effect of Film Hole Row Location," ASME JOURNAL OF TURBOMACHINERY, Vol. 114, pp. 716–723.

Ou, S., Han, J. C., Mehendale, A. B., and Lee., C. P., 1994, "Unsteady Wake Over a Linear Turbine Blade Cascade With Air and CO_2 Film Injection: Part I—Effect on Heat Transfer Coefficients," ASME JOURNAL OF TURBOMACHINERY, Vol. 116, pp. 721–729.

Takeishi, K., Aoki, S., Sato, T. and Tsukagoshi, K., 1992, "Film Cooling on a Gas Turbine Rotor Blade," ASME JOURNAL OF TURBOMACHINERY, Vol. 114, pp. 828–834.

APPENDIX A

In this appendix, we show that the parameters adopted in this study almost match those encountered in a real turbomachine.

Table A.1 shows comparisons between several normalized parameters for a real turbomachine and the present study. As for an incident turbulence intensity to turbine rotor blades, the analytical approach is as follows.

Along a steady streamline away from the blade surfaces, turbulence kinetic energy k is governed by

$$\frac{Dk}{Dt} = -\epsilon, \tag{A.1}$$

where ϵ is the dissipation rate and can be calculated from the relationship $\epsilon = k^{3/2}/L_\epsilon$, prescribing the mixing length L_ϵ. Assuming steady flow and isotropic turbulence, we have

$$\frac{D}{Dt} = U_s \frac{\partial}{\partial x_s}, \tag{A.2}$$

$$k = 1.5(U_s \cdot Tu)^2, \tag{A.3}$$

where U_s represents the streamwise velocity along the streamline. Equation (A.1) can be integrated between nozzle inlet (x_{so}) and nozzle exit (x_s) to yield the turbulence intensity at the nozzle exit as follows,

Table A.1 Comparison between several normalized parameter for a real turbomachine and the present study

	Real turbomachine	Present study
Reynolds number Re_D	$10^4 \sim 10^6$	14.1×10^4
Strouhal number S	0.2 ~ 0.4	0.22 ~ 0.37
Turbulence intensity Tu	3 ~ 5%	1.5 ~ 4 %

$$k(x_s) = k(x_{so}) - \int_{x_{so}}^{x_s} \frac{\epsilon dx'}{U(x')}. \tag{A.4}$$

Taking account of the experimental finding by Goebel et al. (1993) that the turbulence intensity at the exit of combustor was around 10–15 percent on the average, we can roughly estimate the turbulence intensity at nozzle exit from Eq. (A.4), which is easily converted into the value in the coordinate system fixed to the rotor blade as presented in Table A.1. This shows the test conditions almost match the real case.

APPENDIX B

Applying the Bernoulli equation to a streamtube between the plenum chamber within the model and the exit of a cooling hole, we have the generic expression as follows:

$$P_2 = p_{out} + \frac{\rho}{2} v_{out}^2 + \left(\zeta_{in} + \lambda \frac{l}{d}\right) \frac{\rho}{2} v_{out}^2, \tag{B.1}$$

where P_2 = total pressure in the chamber, p_{out} = hole exit static pressure, v_{out} = mean velocity in the tube, ζ_{in} = inlet loss coefficient, λ = friction coefficient, l = tube length, d = tube inner diameter. From this equation, mean injection velocities from the cooling holes of the first and second rows are calculated by

$$v_{15} = \sqrt{\frac{2(P_2 - p_{15})}{\rho\left(1 + \zeta_{in} + \lambda \frac{l_{15}}{d}\right)}} = \sqrt{\frac{2(P_2 - p_\infty + p_\infty - p_{15})}{\rho\left(1 + \zeta + \lambda \frac{l_{15}}{d}\right)}}, \tag{B.2}$$

$$v_{40} = \sqrt{\frac{2(P_2 - p_{15})}{\rho\left(1 + \zeta_{in} + \lambda \frac{l_{40}}{d}\right)}} = \sqrt{\frac{2(P_2 - p_\infty + p_\infty - p_{15})}{\rho\left(1 + \zeta_{in} + \lambda \frac{l_{40}}{d}\right)}}. \tag{B.3}$$

From the experiment by Funazaki (1996), it was found that the velocity distribution near the stagnation could be approximated by that of the potential flow around the circular cylinder. Consequently, p_{15} and p_{40} can be given by

$$p_\infty - p_{15} = -0.732 \frac{\rho}{2} U_\infty^2, \tag{B.4}$$

$$p_\infty - p_{40} = 0.653 \frac{\rho}{2} U_\infty^2, \tag{B.5}$$

where p_∞ is the free-stream static pressure upstream of the test model. From Eqs. (B.2) ~ (B.5),

$$\frac{v_{15}}{U_\infty} = -\frac{\sqrt{C_{p2} - 0.732}}{\sqrt{1 + \zeta_{in} + \lambda \frac{l_{15}}{d}}}, \tag{B.6}$$

$$\frac{v_{40}}{U_\infty} = \frac{\sqrt{C_{p2} - 0.653}}{\sqrt{1 + \zeta_{in} + \lambda \frac{l_{40}}{d}}}, \tag{B.7}$$

$$C_p = \frac{P_2 - p_\infty}{\frac{\rho}{2} U_\infty^2}. \quad \text{(B.8)}$$

From the definition of the blowing ratio B, also considering that the air density ratio of the mainstream and secondary air is about unity, we have

$$B = \frac{\rho_2 U_2}{\rho_\infty U_\infty} = \frac{U_2}{U_\infty} = \frac{1}{U_\infty} \left\{ \frac{n_{15} v_{15} + n_{40} v_{40}}{n_{15} + n_{40}} \right\}. \quad \text{(B.9)}$$

where n_{15} and n_{40} are numbers of cooling holes of the first and second rows. Accordingly, B is expressed by the following equation:

$$B = \frac{\sqrt{C_p}}{(n_{15} + n_{40}) \sqrt{1 + \zeta_{in} + \lambda \frac{l}{d}}} \times \left\{ n_{15} \sqrt{1 - \frac{0.732}{C_p}} + n_{40} \sqrt{1 + \frac{0.653}{C_p}} \right\}. \quad \text{(B.10)}$$

Local blowing ratio $\bar{B}$, defined as

$$\bar{B} = \frac{\rho_2 v_{out}}{\rho_\infty U_{local}} = \frac{v_{out}}{U_{local}} = \frac{v_{out}}{U_\infty} \cdot \frac{U_\infty}{U_{local}}, \quad \text{(B.11)}$$

can be finally obtained as a function of B, from Eq. (B.6) or (B.7) and Eq. (B.10) (using C_p as a parameter B).